

A Novel Boundary Element Method Using Surface Conductive Absorbers for Full-Wave Analysis of 3-D Nanophotonics

Lei Zhang, *Student Member, IEEE*, Jung Hoon Lee, Ardavan Oskooi, Amit Hochman, *Member, IEEE*, Jacob K. White, *Fellow, IEEE*, and Steven G. Johnson

Abstract—Fast surface integral equation (SIE) methods seem to be ideal for simulating 3-D nanophotonic devices, as such devices generate fields in both the interior device volume and in the infinite exterior domain. SIE methods were originally developed for computing scattering from structures with finite surfaces, and since SIE methods automatically represent the infinite extent of the exterior scattered field, there was no need to develop numerical absorbers. Numerical absorbers are needed when SIE methods are used to simulate nanophotonic devices that process or couple light, to provide nonreflecting termination at the optical ports of such devices. In this paper, we focus on the problem of developing an approach to absorbers that are suitable for port termination, yet preserve the surface-only discretization and the geometry-independent Green's function properties of the SIE methods. Preserving these properties allows the absorber approach to be easily incorporated in commonly used fast solvers. We describe our solution to the absorber problem, that of using a gradually increasing surface conductivity, and show how to include surface conductivity in SIE methods. We also analyze numerical results using our absorber approach to terminate a finite-length rectangular cross section dielectric waveguide. The numerical results demonstrate that our surface-conductivity absorber can easily achieve a reflected power of less than 10^{-7} , and that the magnitude of the transition reflection is proportional to $1/L^{2d+2}$, where L is the absorber length and d is the order of the differentiability of the surface conductivity function.

Index Terms—Boundary element method, nanophotonics, reflections, surface conductive absorber, surface integral equation.

Manuscript received May 23, 2010; revised September 29, 2010, December 29, 2010; accepted January 03, 2011. Date of publication January 20, 2011; date of current version March 14, 2011. This work was supported in part by the Singapore-MIT Alliance (SMA), in part by the MARCO Focus Center on Interconnect, in part by the Dr. Dennis Healy of DARPA MTO under Award N00014-05-1-0700 administered by the Office of Naval Research, and in part by the Army Research Office through the Institute for Soldier Nanotechnologies under Contract DAAD-19-02-D0002.

L. Zhang, A. Hochman, and J. K. White are with the Department of Electrical Engineering and Computer Science, Massachusetts Institute of Technology, Cambridge, MA 02139 USA. (e-mail: zhangl@alum.mit.edu; hochman@mit.edu; white@mit.edu).

J. H. Lee is with Applied Computer Science and Mathematics, Merck & Company, Inc., Rahway, NJ 07065 USA (e-mail: jung_hoon_lee@merck.com).

A. Oskooi is with Kyoto University, Kyoto 615-8510, Japan (e-mail: ardfar@mit.edu).

S. G. Johnson is with the Department of Mathematics, Massachusetts Institute of Technology, Cambridge, MA 02139 USA. (e-mail: stevenj@math.mit.edu).

Color versions of one or more of the figures in this paper are available online at <http://ieeexplore.ieee.org>.

Digital Object Identifier 10.1109/JLT.2011.2107727

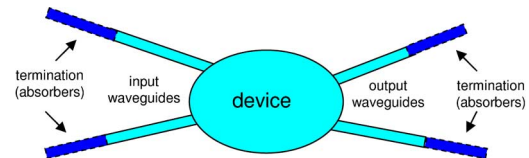


Fig. 1. Schematic diagram of a photonic device with input and output waveguide channels, which must be truncated in a surface integral equation method.

I. INTRODUCTION

IN this paper, we describe an absorber technique for terminating optical waveguides that is easily combined with surface integral equation (SIE) methods, which otherwise have difficulties with waveguides, and other surfaces, that extend to infinity. As an example of our technique, in order to attenuate the waves reflected from a truncated waveguide, we append the waveguide with an absorbing region with a gradually increasing surface conductivity, as diagrammed in Fig. 1. The transition between the waveguide and the appended absorbing region still generates reflections, but those reflections can be minimized by making the transition between regions as smooth as possible. We show how this smoothness can be achieved by smoothly changing the SIE boundary conditions in the absorber region. Our numerical experiments demonstrate that the reflections from our method are orders of magnitude smaller than those produced by the most straightforward method for generating absorbers for SIE methods, that of appending the truncated waveguide with a long absorbing region with a fixed small volumetric loss. In addition, we demonstrate that when using our surface-conductivity absorber, the computed transition reflections satisfy an asymptotic power-law behavior as a function of length, where the power law is determined by the smoothness of the waveguide-absorber transition [1].

One important advantage of SIE methods is that they treat infinite homogeneous regions (and some other cases) analytically via Green's functions, so for problems with finite surfaces (for example, scattering from a finite-sized body) there is no need to artificially truncate space. A second important advantage of SIE methods is that only surfaces need be discretized, so the method can be computationally efficient for problems with piecewise homogeneous material properties. The most commonly used SIE method is the method-of-moments, also referred to as the boundary-element method (BEM) [2]–[6], and the popularity of

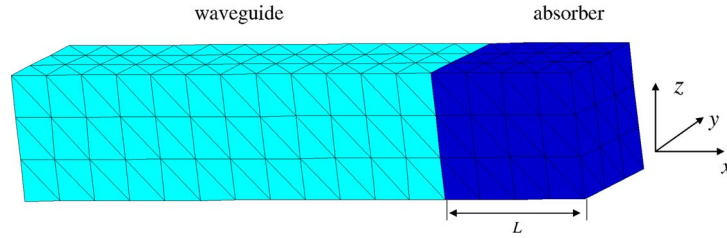


Fig. 2. Discretized dielectric waveguide with an absorber attached.

these methods has increased substantially since the development of fast $O(N \log N)$ solvers [7]–[12].

A difficulty arises when applying SIE methods to structures with unbounded surfaces, such as infinitely extended channels, a typical problem in photonics. Fig. 1 is a generic photonic device diagram, with finite-length waveguide channels whose free ends, representing the device's optical ports, are terminated by absorbers. In order to accurately simulate and characterize such a device, the finite-length channels must either be extended to infinity, obviously requiring infinite computational resources, or absorbers must be appended to the end of the finite-length channels, to eliminate reflections due to geometric truncation. For volume methods, such as finite-difference (FDM) and finite-element methods (FEM), there is a rich literature on absorber techniques [13]–[18], but techniques for including absorbers in SIE methods have received little attention. This is primarily because SIE methods were originally developed for finite-body scattering problems, where SIE methods do not require absorbers.

Absorbers are needed when using SIE methods to analyze photonic crystals, geometrically periodic waveguides, and ring resonators [19], [20], and this has boosted interest in developing SIE-specific absorber techniques. Strategies that have been examined include using a continuously varying Green's function, as in [21], or using an absorbing region with a spatially varying volume conductivity, and then combining the SIE method with a volume integral equation method [22] in the absorber region. It is also possible to create an absorber for SIE methods by coupling the method to an FEM- or FDM-based method.

Using an absorber that is based on a geometry-specific Green's function makes it challenging to develop a general purpose fast solver for photonics, and an absorber based on coupling an SIE method to a method based on volume discretization requires special techniques to avoid generating reflections from the change in discretization techniques. Instead, we developed an absorber strategy that retains the desirable SIE method properties of surface-only discretization and the desirable property of geometry-independent (but not material independent) Green's functions, the options for absorbers seem quite limited. For waveguides, one obvious possibility is to append the waveguide with a long, slightly lossy, absorbing region. For example, consider the finite rectangular waveguide to which an absorber with constant volume electrical conductivity σ_E and magnetic conductivity σ_M is attached, as shown in Fig. 2. The longitudinal cross section of this arrangement is shown in Fig. 3(a). The lengths of the waveguide and absorber are $20\lambda_i$ and $10\lambda_i$, where λ_i is the wavelength in the interior medium. To achieve small reflections, the intrinsic impedance of the

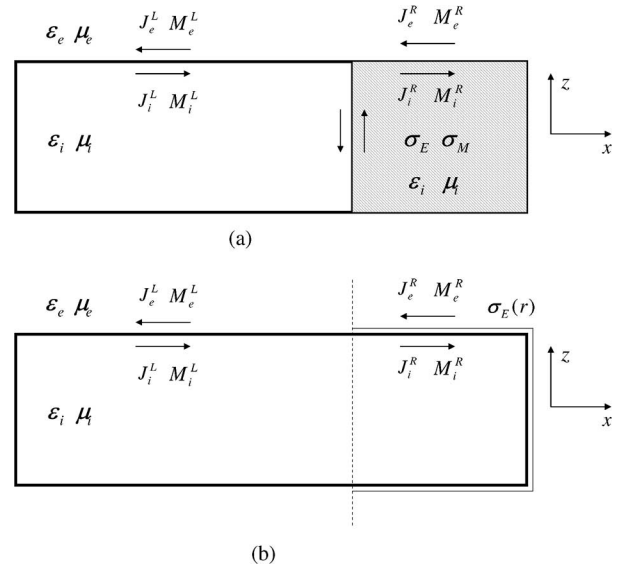


Fig. 3. 2-D longitudinal section of a waveguide with an absorber. Lengths of the waveguide and absorber are $20\lambda_i$ and $10\lambda_i$, respectively, with λ_i denoting the wavelength in the waveguide medium. The waveguide cross section size is $0.7211\lambda_i \times 0.7211\lambda_i$. Relative permittivities of the waveguide (silicon) and the external medium (air) are 11.9 and 1, respectively. (a) Waveguide with a volume absorber. (b) Waveguide with a surface absorber.

absorber is matched to that of the waveguide. Hence, the volume electrical conductivity σ_E and the volume magnetic conductivity σ_M satisfy $\sigma_E/\sigma_M = \epsilon_i/\mu_i$, where ϵ_i and μ_i are the permittivity and permeability of both the waveguide and absorber media, respectively. For this waveguide example, we can quantify the effectiveness of the absorber by numerically evaluating the standing wave ratio (SWR), and then applying standard transmission line theory to determine the reflection coefficient from the SWR. The smaller the reflection coefficient, the more effective the absorber. For this waveguide plus volume absorber example, the SWR was evaluated by computing the ratio of the maximum field magnitude to the minimum field in the waveguide, on the waveguide axis nearest the waveguide-absorber interface. Using hand-optimized values for σ_E (0.0023 S/m) and σ_M , respectively, the smallest reflection coefficient obtained for a $10\lambda_i$ length volume absorber was 2.5%. This value, also listed in the first column of Table I, is unacceptably high for many design applications. In particular, the taper design example shown in [19] requires that the truncation-related reflections be smaller than 10^{-3} . To achieve such high accuracy with a fixed loss volume absorber would require an impractically long absorber.

In this paper, we examine an alternative approach to absorbers. We add electrical conductivity to the waveguide surface rather than to the volume, via a delta-function conductivity

TABLE I
STANDING WAVE RATIO (SWR) AND FIELD REFLECTION COEFFICIENT FOR A VOLUME ABSORBER AND TWO SURFACE-CONDUCTIVITY ABSORBERS (LINEAR AND QUADRATIC). THE SWR IS COMPUTED IN INSIDE THE $20\lambda_z$ LONG WAVEGUIDE, NEAR ITS INTERFACE WITH THE $10\lambda_z$ LONG ABSORBER. SEE FIG. 4 FOR THE CORRESPONDING ELECTRICAL FIELD PLOTS FOR THE SURFACE ABSORBER CASES

Absorber type	Volume Absorber	Surface Absorber	
Conductivity profile	Constant	Linear	Quadratic
SWR	1.0503	1.0022	1.0002
Reflect. Coeff. r	0.0246	0.0011	1.0378×10^{-4}

on the absorber surface, as shown in Fig. 3(b). The absorber's interior medium remains the same as the waveguide's, thus eliminating the need to discretize the waveguide-absorber interface, shown as a solid line in Fig. 3(a) and a dashed line in Fig. 3(b). This surface conductivity could produce transition reflection at the interface, since it is obviously not a PML-type strategy, however, the surface-conductivity strategy permits a surface-only discretization, leaves the Green's functions unaltered, yet allows for a smoothly increasing surface conductivity useful for reducing transition reflections. Specifically, the surface conductivity is easily implemented in an SIE method as it corresponds to a jump discontinuity in the field boundary conditions at the absorber surface. Since the SIE explicitly discretizes the surface boundary, continuously varying the field boundary conditions is easily implemented.

As a preview of results to be described later, in Fig. 4, we show the numerically computed complex magnitudes of the electric field along the x direction inside a rectangular waveguide and in the absorber for two different surface conductivity profiles. For this example, $0 < x < x_0$ correspond to points inside the waveguide region, $x_0 < x < (x_0 + L)$ correspond to points inside the surface absorber region, and L is the length of the absorber. The surface electrical conductivity in this region is given by $\sigma_E(x) = \sigma_0[(x - x_0)/L]^d$, where $d = 1$ and $d = 2$ generate linear and quadratic surface-conductivity profiles, respectively. The constant σ_0 is determined by matching the total attenuation over the length of surface-conductivity absorber to the total attenuation of the aforesaid optimized volume absorber. The approach for calculating the attenuation along the absorber is given in Section IV-A.

In the complex magnitude plots of Fig. 4, the peak-to-peak magnitudes of the ripples are an indication of the magnitude of the reflections. As is easily seen in Fig. 4, the reflections are visible when using a linearly increasing surface conductivity, and are almost invisibly small for quadratically increasing surface conductivity. The magnitudes of the field reflection coefficients r are listed in Table I, and show that the reflection coefficient for the quadratically varying surface conductivity is nearly one thousand times smaller than the reflection coefficient for the volume absorber. The results for the linearly and quadratically varying surface absorber verify the results in [1], that the smoothness of any transition in a waveguide, largely determines the resulting reflection.

This paper is organized as follows. In Section II, the BEM formulation incorporating surface conductivity is derived. In Section III, the decay rate due to the surface conductivity is examined using both numerical experiments and calculations

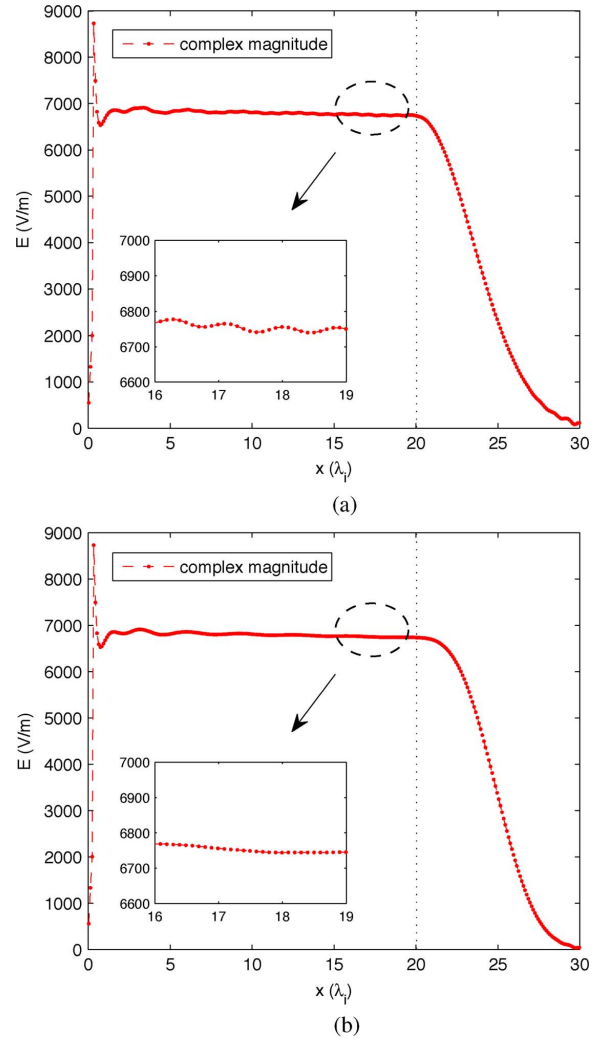


Fig. 4. Complex magnitude of the electric field inside a waveguide and the attached surface absorber. Dashed line indicates the position of the waveguide-absorber interface. Lengths of the waveguide and absorber are $20\lambda_z$ and $10\lambda_z$, respectively, with λ_z denoting the wavelength in the waveguide medium. See Table I for the corresponding numerically measured reflection coefficients. (a) Linear surface conductivity along x direction ($d = 1$). (b) Quadratic surface conductivity along x direction ($d = 2$).

based on perturbation theory and on Poynting's theorem. In Section IV, the asymptotic behavior of transition reflections with respect to absorber length is presented. In Section V, we note the existence of radiation modes originating from the mismatch of the excitation source and the waveguide mode, and show that the radiation complicates the interpretation of certain numerical results, but does not affect the performance of the surface absorber. Details of the numerical implementation of the SIE solver are given in the Appendix, including a description of BEM matrix construction, the preconditioning iterative matrix solution technique, and FFT-based acceleration of the matrix-vector products.

II. BEM FORMULATIONS WITH THE SURFACE CONDUCTIVE ABSORBER

In this section, we describe the 3-D BEM formulation for a waveguide truncated with a surface conductive absorber. Fig. 3(b) shows the x - z plane cross section of an x -directed

truncated rectangular waveguide, where the surface conductive absorber region is to the right of the dashed line. The permittivity and permeability of the waveguide interior and the exterior media are denoted as ϵ_e, μ_e and ϵ_i, μ_i , where the subscripts e and i denote the exterior and the interior, respectively. The electrical surface conductivity $\sigma_E(\mathbf{r})$ is subscripted with E as a reminder that only electrical conductivity is being considered, though the generalization of what follows to both electrical and magnetic conductivity could be considered. As is described in Section III, using only electrical conductivity can have a saturation phenomenon that can be avoided at the cost of using a longer absorber. The system is excited by a Gaussian beam propagating in $+\hat{x}$ direction. The Gaussian beam is generated by a dipole in a complex space [23], where the real part of the dipole position is inside the waveguide, $0.25\lambda_i$ from the left end. In this paper, the convention of the $e^{j\omega t}$ time-harmonic mode is adopted.

In SIE methods, for computing time-harmonic solutions, the unknowns are surface variables. In our case, we use surface electrical and magnetic currents on both the interior, \mathbf{J}_i and \mathbf{M}_i , and exterior, \mathbf{J}_e and \mathbf{M}_e , of every surface. The currents on surfaces with $\sigma_E = 0$ on the left side of Fig. 3(b), satisfy a simpler set of equations than the currents on surfaces where $\sigma_E \neq 0$, the right side of Fig. 3(b). When appropriate, we distinguish between the $\sigma_E = 0$ and $\sigma_E \neq 0$ currents with superscripts L and R , respectively.

Invoking the equivalence principle [24] yields a relation between surface currents and fields

$$-\hat{n} \times \mathbf{E}_e = \mathbf{M}_e \quad (1)$$

$$\hat{n} \times \mathbf{H}_e = \mathbf{J}_e \quad (2)$$

$$\hat{n} \times (\mathbf{E}_i + \mathbf{E}_{\text{inc}}) = \mathbf{M}_i \quad (3)$$

$$-\hat{n} \times (\mathbf{H}_i + \mathbf{H}_{\text{inc}}) = \mathbf{J}_i \quad (4)$$

where \hat{n} is an exterior-directed normal unit-vector, \mathbf{E}_{inc} and \mathbf{H}_{inc} are the electric and magnetic fields of the Gaussian beam in a homogeneous space with material parameters equal to those of the waveguide interior, and $\mathbf{E}_e, \mathbf{H}_e$ and $\mathbf{E}_i, \mathbf{H}_i$ are electric and magnetic fields due to the equivalent currents in the exterior and interior, respectively.

On the surface of the waveguide, the continuity of the tangential components of the electric and magnetic fields yields the well-known PMCHW formulation [2], [3]

$$\begin{aligned} \hat{n} \times \mathbf{E}_e^L(\mathbf{J}_e^L, \mathbf{M}_e^L, \mathbf{J}_e^R, \mathbf{M}_e^R) \\ = \hat{n} \times [\mathbf{E}_e^L(\mathbf{J}_i^L, \mathbf{M}_i^L, \mathbf{J}_i^R, \mathbf{M}_i^R) + \mathbf{E}_{\text{inc}}^L] \end{aligned} \quad (5)$$

$$\begin{aligned} \hat{n} \times \mathbf{H}_e^L(\mathbf{J}_e^L, \mathbf{M}_e^L, \mathbf{J}_e^R, \mathbf{M}_e^R) \\ = \hat{n} \times [\mathbf{H}_e^L(\mathbf{J}_i^L, \mathbf{M}_i^L, \mathbf{J}_i^R, \mathbf{M}_i^R) + \mathbf{H}_{\text{inc}}^L] \end{aligned} \quad (6)$$

where $\mathbf{E}^L(\cdot)$ and $\mathbf{H}^L(\cdot)$ are integral operators described in the Appendix. From (1)–(4) and the tangential field continuity in the surface conductivity free region, the equivalent currents on the two sides of the waveguide surface are of the equal magnitude, but are opposite in direction. Specifically

$$\mathbf{J}_e^L = -\mathbf{J}_i^L = \mathbf{J}^L \quad (7)$$

$$\mathbf{M}_e^L = -\mathbf{M}_i^L = \mathbf{M}^L \quad (8)$$

Thus, the unknown currents on the waveguide side are reduced to \mathbf{J}^L and \mathbf{M}^L .

For the surfaces where $\sigma_E \neq 0$, a modified surface formulation is needed, one that incorporates the discontinuity due to the surface conductivity. When $\sigma_E \neq 0$, the tangential electric field is still continuous across the absorber surface, and therefore

$$\begin{aligned} \hat{n} \times \mathbf{E}_e^R(\mathbf{J}_e^L, \mathbf{M}_e^L, \mathbf{J}_e^R, \mathbf{M}_e^R) \\ = \hat{n} \times [\mathbf{E}_i^R(\mathbf{J}_i^L, \mathbf{M}_i^L, \mathbf{J}_i^R, \mathbf{M}_i^R) + \mathbf{E}_{\text{inc}}^R]. \end{aligned} \quad (9)$$

The tangential magnetic field is not continuous as a sheet of surface electric current $\mathbf{J}_{\text{ind}} = \sigma_E \mathbf{E}_{\text{tan}}^R$ is induced due to the electrical surface conductivity, thus creating a jump. Therefore,

$$\begin{aligned} \hat{n} \times [\mathbf{H}_e^R(\mathbf{J}_e^L, \mathbf{M}_e^L, \mathbf{J}_e^R, \mathbf{M}_e^R) \\ - \mathbf{H}_i^R(\mathbf{J}_i^L, \mathbf{M}_i^L, \mathbf{J}_i^R, \mathbf{M}_i^R) - \mathbf{H}_{\text{inc}}^R] = \sigma_E \mathbf{E}_{\text{tan}}^R \end{aligned} \quad (10)$$

where $\mathbf{E}_{\text{tan}}^R = -\hat{n} \times (\hat{n} \times \mathbf{E}^R)$ is the tangential electric field on the absorber surface, and could choose the field on either side of the absorber surface according to the enforced equality in (9).

As a result of (1), (3), and (9), the interior and exterior magnetic currents can be represented with a single variable

$$\mathbf{M}_e^R = -\mathbf{M}_i^R = \mathbf{M}^R \quad (11)$$

but the discontinuity of tangential magnetic field implies $|\mathbf{J}_e^R| \neq |\mathbf{J}_i^R|$, and (2), (4), and (10) must be combined to generate a local equation

$$\mathbf{J}_e^R + \mathbf{J}_i^R = \sigma_E \mathbf{E}_{\text{tan}}^R \quad (12)$$

Finally, using the integral operator relation between $\mathbf{E}_{\text{tan}}^R$ and \mathbf{J} and \mathbf{M} , and substituting into (10) and (12), yields

$$\begin{aligned} \hat{n} \times [\mathbf{H}_e^R(\mathbf{J}_e^L, \mathbf{M}_e^L, \mathbf{J}_e^R, \mathbf{M}_e^R) \\ - \mathbf{H}_i^R(\mathbf{J}_i^L, \mathbf{M}_i^L, \mathbf{J}_i^R, \mathbf{M}_i^R) - \mathbf{H}_{\text{inc}}^R] \\ = \sigma_E \mathbf{E}_{e,\text{tan}}^R(\mathbf{J}_e^L, \mathbf{M}_e^L, \mathbf{J}_e^R, \mathbf{M}_e^R) \end{aligned} \quad (13)$$

$$\begin{aligned} \mathbf{J}_e^R + \mathbf{J}_i^R \\ = \sigma_E [\mathbf{E}_{i,\text{tan}}^R(\mathbf{J}_i^L, \mathbf{M}_i^L, \mathbf{J}_i^R, \mathbf{M}_i^R) + \mathbf{E}_{\text{inc,tan}}^R]. \end{aligned} \quad (14)$$

The unknowns, the surface currents $\mathbf{J}^L, \mathbf{M}^L, \mathbf{J}_e^R, \mathbf{J}_i^R$ and \mathbf{M}^R , can be determined by solving (5), (6) on the left waveguide surfaces and (9), (13), (14) on the right absorber surfaces. The resulting linear system can be constructed and solved as described in Appendix. It is possible to simplify the formulation by eliminating one extra variable of electric currents on the absorber surface, though there are some accuracy issues [25].

III. FIELD DECAY RATE

In this section, we demonstrate agreement between three methods for computing the exponential decay rate in a region with electrical surface conductivity: direct numerical experiment, perturbation theory, and using Poynting's Theorem. For the purpose of simplifying the comparison, in just this section we use the example of a single dielectric waveguide with a uniformly distributed surface conductivity. The longitudinal cross section is shown in Fig. 5. The behavior of interior fields generated by a Gaussian beam source were computed using a BEM method based on solving (9), (13), and (14).

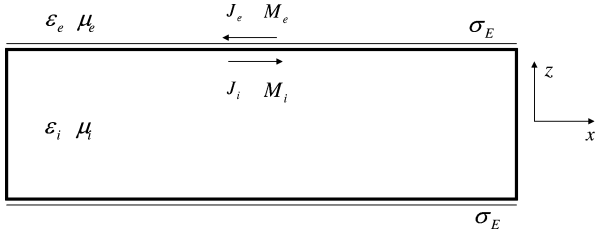


Fig. 5. 2-D longitudinal cross section of a waveguide with uniform surface conductivity. This absorber-only example is used in Section III. Waveguide length is $10\lambda_i$ and cross section size is $0.7211\lambda_i \times 0.7211\lambda_i$. The relative permittivity of the waveguide and external medium are 11.9 and 1, respectively.

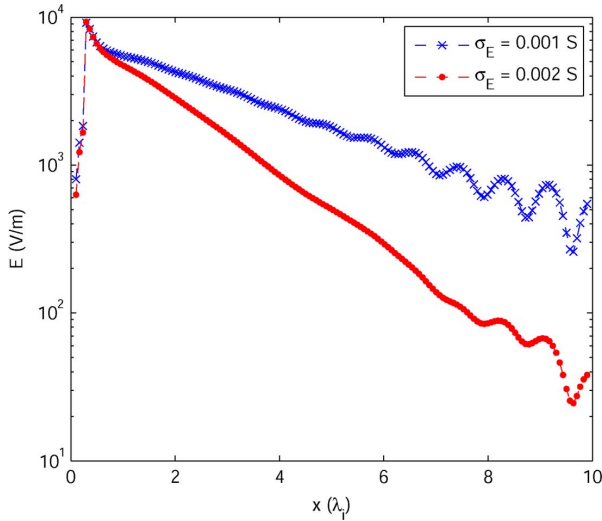


Fig. 6. Complex magnitude of the electric field along x inside the waveguide in Fig. 5 with uniform surface conductivity.

The plots in Fig. 6 show the numerically computed complex magnitudes of the electric fields along the x axis inside the waveguide for two cases, $\sigma_E = 0.001$ S and $\sigma_E = 0.002$ S. As expected, the complex magnitude decays exponentially with distance from the source with a surface-conductivity dependent rate. Also, as can be seen, waves reflect back from the right end and presumably these reflections decay as they travel to the left.

An approximation to the rate of exponential decay can be determined by fitting the field plots. The fitted decay rates for a range of σ_E are shown in Fig. 7 and denoted with a dashed star curve. The decay rate does not monotonically increase with the surface conductivity. The curve shape can be explained as follows. When σ_E is small, the propagating wave is able to penetrate the lossy surface and is absorbed, with the absorption increasing with σ_E as expected. However, for large σ_E , the surface conductor itself becomes reflecting, forming essentially an enclosed metallic waveguide; as $\sigma_E \rightarrow \infty$ the tangential electric field vanishes at the surface and therefore there is no absorption. The practical implications of this upper bound on effective values for σ_E are limited, and are described in Section IV.

The following sections introduce two alternative approaches to calculate the decay rate from surface conductivities, to confirm and further illustrate the aforementioned numerical observations.

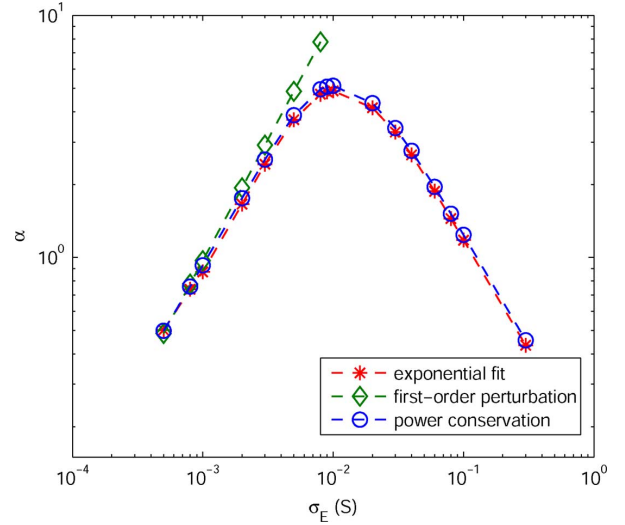


Fig. 7. Comparison of three methods for computing the rate of field exponential decay along the propagation direction versus surface conductivity.

A. Decay Rate Calculation by Perturbation Theory

In this section, a first-order closed-form decay rate formula, valid for small surface conductivity, is derived using perturbation theory. Assume the electric field $\mathbf{E}^{(0)}(\mathbf{r})$ of the fundamental mode of a lossless rectangular waveguide is given, and the superscript (0) denotes the unperturbed quantity. When electrical surface conductivity σ_E is put on the waveguide surface, it is equivalent to a perturbation of permittivity, denoted as $\Delta\epsilon(\mathbf{r}) = -(j\sigma_E/\omega)\delta_S(\mathbf{r})$, where δ_S is the Dirac delta function across the waveguide surface. According to [24], [26], the first-order variance of angular frequency due to the perturbation of permittivity $\Delta\epsilon(\mathbf{r})$ is

$$\Delta\omega^{(1)} = -\frac{\omega}{2} \frac{\int_V \Delta\epsilon(\mathbf{r}) |\mathbf{E}^{(0)}(\mathbf{r})|^2 dV}{\int_V \epsilon |\mathbf{E}^{(0)}(\mathbf{r})|^2 dV} \quad (15)$$

where V is the whole volume domain and the superscript (1) denotes a first-order approximation. After applying the triple product rule to the partial derivatives of the three interdependent variables ω, k, σ_E , we obtain a first-order change in propagation constant k due to the frequency change in (15), denoted as $\Delta k^{(1)} = -\Delta\omega/V_g$, where V_g is the group velocity, as $V_g = (\partial\omega/\partial k)|_{\sigma_E}$ in which the subscript indicates σ_E is held fixed. Combining (15) and aforementioned equations of $\Delta\epsilon(\mathbf{r})$ and $\Delta k^{(1)}$, the integral in the numerator of (15) is reduced to a surface integral of the tangential components of the electric field, therefore

$$\Delta k^{(1)} = -\frac{j\sigma_E}{2V_g} \frac{\int_S |\mathbf{E}_{\text{tan}}^{(0)}(\mathbf{r})|^2 dS}{\int_V \epsilon |\mathbf{E}^{(0)}(\mathbf{r})|^2 dV} \quad (16)$$

where S is the surface of the waveguide. As expected, the perturbation in the propagation constant is imaginary, which in turn represents the decay rate $\alpha^{(1)} = -\text{Im}\{\Delta k^{(1)}\}$. With a uniform cross section, the volume and surface integrals in (16) can be further reduced to surface and line integrals on the cross section, respectively. The electric field before the perturbation $\mathbf{E}^{(0)}(\mathbf{r})$,

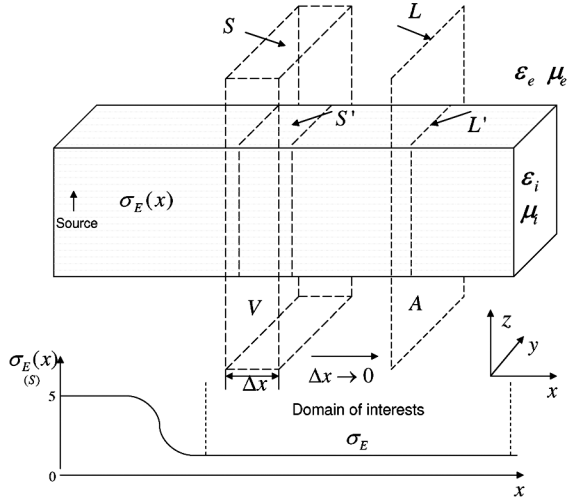


Fig. 8. Illustration of the approach using Poynting's theorem to calculate the decay rate of a waveguide with surface conductivity. Plot of the surface conductivity distribution $\sigma_E(x)$ along the longitudinal direction is aligned with the waveguide.

along with V_g , can be obtained numerically, for example, with a plane-wave method [27].

The decay rate calculated using the perturbation is plotted in Fig. 7 with a dashed diamond curve. Note that the curve overlaps with decay rates computed with other methods when the surface conductivity is small, and deviates for larger conductivity as should be expected given the first-order approximation.

B. Decay Rate Calculation Using Poynting's Theorem

The aforesaid perturbation method predicts the decay rate when the surface conductivity is small. An alternative approach, based on Poynting's theorem, can be used to calculate the decay rate for the entire σ_E range.

Fig. 8 shows a waveguide with surface conductivity and also plots the conductivity function $\sigma_E(x)$ with x axis aligned with the x axis of the waveguide. Since this approach requires integrating the fields of source-excited propagating modes in the exterior region, some inevitably excited modes, such as radiation modes that will be discussed in Section V, must be suppressed. For this reason, the surface conductivity starts with a large constant value (5 S). The large surface conductivity leads to the saturation as seen in Fig. 7, and therefore, the Gaussian-beam source excites metallic waveguide modes at the beginning, propagating in $+\hat{x}$ direction in the closed interior region. The surface conductivity is then smoothly reduced to a smaller value, with which the decay rate is to be calculated. In this way, the metallic waveguide modes can smoothly change to the desired decaying dielectric waveguide modes with minimal radiation modes excited.

The decaying propagating mode in the domain of interest, shown in Fig. 8, is assumed in the form

$$\mathbf{E}(\mathbf{r}) \sim \mathbf{E}_0(y, z)e^{-\alpha x - j\beta x} \quad (17)$$

$$\mathbf{H}(\mathbf{r}) \sim \mathbf{H}_0(y, z)e^{-\alpha x - j\beta x} \quad (18)$$

where β is the real propagation constant, and α is the unknown decay rate. The Poynting vector in frequency domain is given by $\mathbf{S} = (1/2)\mathbf{E} \times \mathbf{H}^*$, and together with the assumed forms of \mathbf{E} in (17) and \mathbf{H} in (18), the derivative with respect to x is given by

$$\frac{d\mathbf{S}}{dx} = -2\alpha\mathbf{S}. \quad (19)$$

As illustrated in Fig. 8, apply Poynting's theorem in the closed volume V

$$\text{Re} \int_S \mathbf{S} \cdot \hat{n} dS = -\frac{1}{2} \int_{S'} \sigma_E |\mathbf{E}_{\text{tan}}|^2 dS' \quad (20)$$

where S is the surface of the volume V , \hat{n} is an exterior-directed normal unit-vector, and S' is the waveguide surface within V . In the limit as $\Delta x \rightarrow 0$, the closed integration surface S becomes a surface A , and one component of the integrand of the left side of (20) becomes $(d\mathbf{S}/dx) \cdot \hat{x}$. Combining (19) and this $\Delta x \rightarrow 0$ limit of (20) yields a closed-form representation of the decay rate α

$$\alpha = \frac{\int_{L'} \sigma_E |\mathbf{E}_{\text{tan}}|^2 dl' + \text{Re} \int_L (\mathbf{E} \times \mathbf{H}^*) \cdot \hat{n} dl}{2 \text{Re} \int_A (\mathbf{E} \times \mathbf{H}^*) \cdot \hat{x} dS} \quad (21)$$

where L denotes the boundary of the surface A , and L' denotes the integral line on the waveguide surface within the surface A .

The decay rate calculated using (21) is plotted in Fig. 7 with a dashed circle curve. It shows good agreement with the decay rate computed using fitting for the entire σ_E range, verifying that the surface conductivity is handled correctly by the BEM in accordance with Maxwell's equations.

IV. REFLECTIONS AND ASYMPTOTIC CONVERGENCE

In this section, we return to the example of a waveguide terminated by an absorber, as shown in Fig. 2. As shown in Section I, a smoothly varying surface conductive absorber easily implemented in the SIE method is orders of magnitude more effective at eliminating reflections than a volume absorber of comparable length. And, since computational cost increases with the length of the absorber, it is worth examining the relationship between reflections and the absorber length. In order to do this, we first require a more careful classification of reflections and a more sensitive numerical measure of reflections than the standing wave ratio method. In the following sections, we will define round-trip and transition reflections and present a measure of the power-law asymptotic convergence of transition reflections.

A. Round-Trip and Transition Reflections

Reflections in a domain of interest can be divided into a round-trip reflection R_r , and a transition reflection R_t . The round-trip reflection is generated by waves entering into the absorber, propagating to the end without being completely absorbed, reflected off the end of the absorber, and eventually propagating back into the waveguide. The round-trip reflection coefficient is proportional to

$$R_r = C e^{-4 \int_L \alpha(x) dx} \quad (22)$$

where the coefficient C is determined by the reflection at the end of the absorber and L is the absorber length. A factor of 2 in the exponent of (22) represents the effect of the round trip, and another factor of 2 indicates that the power is considered.

The transition reflection is the reflection generated by the change in material properties at the waveguide-absorber interface. Therefore, smoother material change at the interface produces smaller transition reflection as predicted by coupled-mode theory [1].

If the round-trip reflection R_r in (22) is held fixed, the decay rate α is inversely related to the absorber length L . In other words, for a longer absorber, a smaller decay rate α can yield the same amount of round-trip reflection. Since α is proportional to the surface conductivity σ_E for small σ_E , using a longer absorber implies a smaller transition reflection. It was further shown in [1] that, given a fixed round-trip reflection, the transition reflection decreased as a power law with increasing absorber length L . The power-law exponent is determined by the order of the differentiability of the medium (conductivity) function. Suppose a conductivity function along x is $\sigma_E(x) = \sigma_0 u((x - x_0)/L)$, where the interface is at $x = x_0$, and $u(s)$ is a monomial function with order d in the $0 \leq s \leq 1$ region

$$u(s) = \begin{cases} s^d, & 0 \leq s \leq 1 \\ 0, & s < 0. \end{cases} \quad (23)$$

With the surface conductivity function $\sigma_E(x)$ and a fixed round-trip reflection, the asymptotic behavior of the transition reflection in terms of the length of the absorber is

$$R_t(L) \sim O\left(\frac{1}{L^{2d+2}}\right). \quad (24)$$

The power-law behavior in (24) indicates that, with a higher order conductivity function, the transition reflection decreases faster with increasing the absorber length. It does not follow that d should be made arbitrarily large, however, there is a tradeoff in which increasing d eventually delays the onset L of the asymptotic regime in which (24) is valid [1].

B. Asymptotic Convergence With L

We present numerical results to verify the asymptotic power-law convergence of the transition reflection of the surface absorber. Because it is hard to explicitly measure the transition reflection in the integral equation method, instead, we measure alternative electric field expressions as in [1].

First, we define $\mathbf{E}(L)$ as the electric field at a fixed position in the waveguide when the length of the absorber is L , with unit λ_i . Thus, $\mathbf{E}(L)$ includes the incident field, the round-trip reflection and the transition reflection. With a small fixed round-trip reflection, the difference of $\mathbf{E}(2L)$ and $\mathbf{E}(L)$ is the difference of the transition reflections, which in the limit of large L approaches to zero, so $\mathbf{E}(2L) - \mathbf{E}(L) \rightarrow 0$. Therefore, $|\mathbf{E}(2L) - \mathbf{E}(L)|$ can be a measure of transition reflection, and specifically, derived from (24), they are subject to the following asymptotic behavior

$$\frac{|\mathbf{E}(2L) - \mathbf{E}(L)|^2}{|\mathbf{E}(L)|^2} \sim O\left(\frac{1}{L^{2d+2}}\right). \quad (25)$$

In the example of a rectangular waveguide attached with a surface absorber, the asymptotic convergence of (25) is shown in

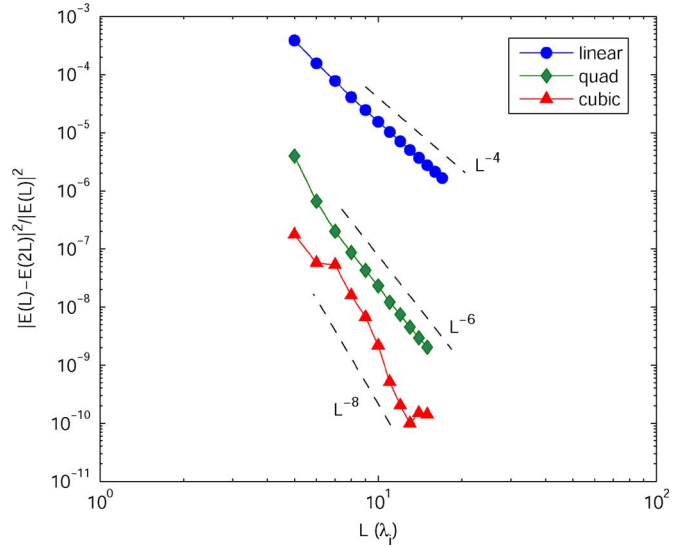


Fig. 9. Asymptotic power-law convergence of the transition reflection with the length of the surface absorber measured using $|\mathbf{E}(2L) - \mathbf{E}(L)|^2/|\mathbf{E}(L)|^2$. Length of the waveguide is $10\lambda_i$, with λ_i denoting the wavelength in the waveguide medium. Waveguide cross section size is $0.7211\lambda_i \times 0.7211\lambda_i$. Relative permittivities of the waveguide (silicon) and the external medium (air) are 11.9 and 1, respectively.

Fig. 9 in a log–log scale for linear, quadratic, and cubic surface conductivity profiles ($d = 1, 2, 3$). In order to keep the same small round-trip reflection, the linear factor σ_0 in the conductivity function should be proportional to $(d + 1)$ and inversely proportional to the length of the absorber [28], as $\sigma_0(L) \sim (d + 1)/L$, and the maximum σ_0 for the shortest absorber length $L = 5\lambda_i$ in our numerical experiment when $d = 1$ is $\sigma_{0,\max} = 0.015$ S. As seen in the figure, the three curves align with the expected L^{-6} , L^{-8} , L^{-10} curves, respectively. The curves would eventually converge to a small quantity, which is the difference of the small round-trip reflections due to a phase difference. The agreement of the figures verifies the power-law behavior of the transition reflection of the surface absorber and further illustrates that a higher order conductivity function leads to smaller transition reflections.

V. RADIATION IN THE SURFACE ABSORBER

A surface absorber with a conductivity that rises smoothly with distance from the waveguide-absorber interface would be expected to have interior fields whose magnitude decays with distance at an accelerating exponential rate. Instead, the field magnitudes decay exponentially near the interface, but then switch to an $O(1/r)$ decay, as shown in Fig. 10. The cause of this switch in decay rate is due to coupled radiation. The radiation is generated by the inevitable mismatch between the excitation source and waveguide modes. The situation is similar to a source radiating in a lossy half-space, in which the dominant field contribution is due to a lateral wave that decays algebraically [29], [30]. Fig. 10 shows the complex magnitude of the interior electric field in a waveguide attached with a long quadratic-profile surface absorber. The waveguide system is excited by a dipole source and a Gaussian beam, respectively, located inside the waveguide. In the semilog plot, the dominant waveguide mode decays at an accelerating exponential rate, and

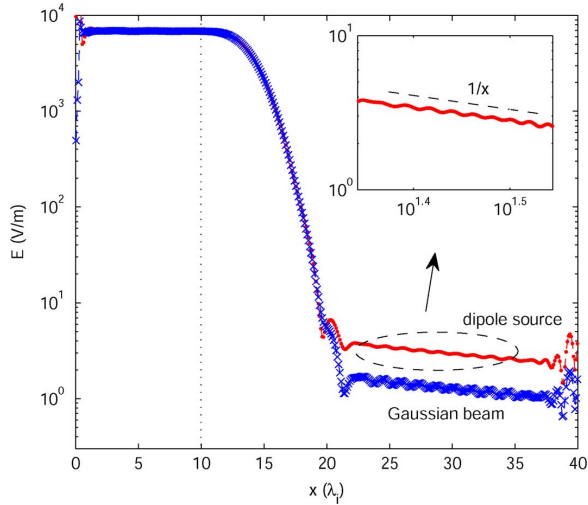


Fig. 10. Complex magnitude of the electric field inside a waveguide and a long surface absorber excited by a dipole source and a Gaussian beam, respectively. Lengths of the waveguide and the absorber are $10\lambda_z$ and $30\lambda_z$, respectively. Surface conductivity on the absorber increases quadratically.

then because the guided mode decays faster than the $O(1/r)$ radiation, the radiation dominates at a certain distance from the waveguide-absorber interface. The coupled radiation results in an $O(1/r)$ floor, as is clearly shown in the inset with a log-log scale. Note that using a Gaussian beam source results in a lower floor than using a dipole source, because the Gaussian beam is more directional, and generates less radiation.

The coupled $O(1/r)$ radiation does not affect the performance of the surface absorber, because the coupled radiation itself is several orders of magnitude smaller than the propagating modes in the waveguide, and little will be reflected. The asymptotic convergence of the transition reflections in Section IV and the 10^{-4} reflection coefficient in Section I consistently show the excellent performance of surface absorbers, obviously unhampered by the effects of radiation.

VI. CONCLUSION

We presented a novel numerical technique, a surface conductive absorber that is easily implemented in the boundary element method, to eliminate the reflections due to the truncation of infinite channels. We illustrated this technique using a dielectric optical waveguide appended with a surface-conductive absorber, and described the modified BEM formulation needed to allow a varying surface conductivity. We further discussed the nonmonotonically increasing decay rate with the surface conductivity and showed agreement between three methods for calculating that decay rate: numerical example, using perturbation theory and Poynting's theorem. We demonstrated that the surface conductive absorber is orders of magnitude more effective than the most obvious approach to generating an absorber that fits with SIE methods, a volume absorber with constant conductivity. Finally, we showed that a waveguide appended by a surface-conductive absorber has a transition reflection that decays as an asymptotic power-law with respect to the length of

the absorber, to verify that the smoothness of conductivity function determines the transition reflection, also noted in [1].

The major advantages of the surface conductive absorber are: 1) the varying surface conductivity is easily implemented in BEM and associated fast solvers and can significantly reduce the transition reflections; 2) the volume properties and of the absorber are the same as the waveguide, so the Green's function is unchanged and there is no interior cross section to discretize, eliminating a potential source of numerical reflections; and 3) there is no change of method at the waveguide/absorber interface, eliminating another potential source of numerical reflections.

In this paper, we focus on presenting this new surface conductive absorber approach using a simple example, a rectangular waveguide. It should be noted that terminating such a simple structure is easily accomplished with a variety of methods. However, our goal is to develop an approach that is general enough that can be used with SIE methods applied to a variety of structures in nanophotonics, like the more complicated periodic photonic crystals. As one final comment, it should be noted that we did not investigate the interaction between wave velocity and surface conductive absorber length. In [28], that issue is examined using a periodic slow-light waveguide, to show that the approach to surface conductive absorbers presented here can result in long absorbers regardless of the conductivity profile.

APPENDIX

A. Construction of a Linear System

From Section II, the five equivalent currents, \mathbf{J}^L , \mathbf{M}^L on the waveguide surfaces, and \mathbf{J}_e^R , \mathbf{J}_i^R , \mathbf{M}^R on the absorber surfaces, are to be determined by solving the (5), (6), (9), (13), and (14). The currents are approximated with the RWG basis function [4] on triangular-meshed surfaces,

$$\mathbf{J} = \sum_m J_m \mathbf{X}_m(\mathbf{r}') \quad (26)$$

$$\mathbf{M} = \sum_m M_m \mathbf{X}_m(\mathbf{r}') \quad (27)$$

where $\mathbf{X}_m(\mathbf{r}')$ is the RWG function on the m th triangle pair, and J_m , M_m are the corresponding coefficients for the electric and magnetic currents, respectively. These unknown coefficients of the five equivalent currents assemble a vector \mathbf{x} to be solved for, specifically,

$$\mathbf{x} = [J^L \quad M^L \quad J_e^R \quad J_i^R \quad M^R]^T. \quad (28)$$

Electric and magnetic fields are represented using the mixed-potential integral equation (MPIE) [5] for a low-order singularity, with integral operators L and K as in [6]

$$\mathbf{E}_l^t(\mathbf{J}, \mathbf{M}) = -Z_l L_l^t(\mathbf{J}) + K_l^t(\mathbf{M}) \quad (29)$$

$$\mathbf{H}_l^t(\mathbf{J}, \mathbf{M}) = -K_l^t(\mathbf{J}) - \frac{1}{Z_l} L_l^t(\mathbf{M}) \quad (30)$$

where $Z_l = \sqrt{\mu_l/\epsilon_l}$ is the intrinsic impedance, the subscript $l = e$ or i denotes the exterior or interior region, and the superscript

$t = L$ or R denotes the waveguide or absorber surfaces. The integral operators on the m th RWG function are given by

$$L_l^t(\mathbf{X}_m) = jk_l \int_{S'} \left[\mathbf{X}_m(\mathbf{r}') + \frac{1}{k_l^2} \nabla \nabla' \cdot \mathbf{X}_m(\mathbf{r}') \right] \times G_l(\mathbf{r}, \mathbf{r}') dS' \quad (31)$$

$$K_l^t(\mathbf{X}_m) = - \int_{S'} \nabla \times G_l(\mathbf{r}, \mathbf{r}') \mathbf{X}_m(\mathbf{r}') dS' \quad (32)$$

where S' is the surface of the m th triangle pair, $k_l = \omega \sqrt{\mu_l \epsilon_l}$ is the propagation constant in region l , and $G_l(\mathbf{r}, \mathbf{r}')$ is the free-space Green's function in region l

$$G_l(\mathbf{r}, \mathbf{r}') = \frac{e^{-jk_l |\mathbf{r} - \mathbf{r}'|}}{4\pi |\mathbf{r} - \mathbf{r}'|} \quad (33)$$

where \mathbf{r} and \mathbf{r}' are target and source positions, respectively.

We employ Galerkin method [31] on the waveguide by using the RWG function as the testing function on target triangle pairs. The tested L, K operators on the n th target triangle pair due to the m th source triangle pair become

$$\mathcal{L}_{l,nm}^t(\mathbf{X}_m) = \int_S \mathbf{X}_n(\mathbf{r}) \cdot L_l^t(\mathbf{X}_m) dS \quad (34)$$

$$\mathcal{K}_{l,nm}^t(\mathbf{X}_m) = \int_S \mathbf{X}_n(\mathbf{r}) \cdot K_l^t(\mathbf{X}_m) dS \quad (35)$$

where S is the surface of the n th target triangle pair. Substituting the tested field operators into (5), (6) yields a matrix \mathbf{A}_{LL} due to the currents $\mathbf{J}^L, \mathbf{M}^L$, and a matrix \mathbf{A}_{LR} due to the currents $\mathbf{J}_e^R, \mathbf{J}_i^R, \mathbf{M}^R$.

On the absorber surfaces, the term $\sigma_E(\mathbf{r}) \mathbf{E}_{i,\text{tan}}^R$ in (13) and (14) requires another testing procedure in order to incorporate the surface conductivity

$$\mathcal{L}_{l,nm}^{R\sigma_E}(\mathbf{X}_m) = \int_S \sigma_E(\mathbf{r}) \mathbf{X}_n(\mathbf{r}) \cdot L_l^R(\mathbf{X}_m) dS \quad (36)$$

$$\mathcal{K}_{l,nm}^{R\sigma_E}(\mathbf{X}_m) = \int_S \sigma_E(\mathbf{r}) \mathbf{X}_n(\mathbf{r}) \cdot K_l^R(\mathbf{X}_m) dS. \quad (37)$$

Similarly, substituting the aforementioned four tested integral operators into (9), (13), and (14) generate a matrix \mathbf{A}_{RL} due to the currents $\mathbf{J}^L, \mathbf{M}^L$, and a matrix \mathbf{A}_{RR} due to the currents $\mathbf{J}_e^R, \mathbf{J}_i^R, \mathbf{M}^R$.

Assembling the four matrices according to (5), (6), (9), (13), and (14) yields a dense linear system

$$\mathbf{A} \mathbf{x} = \mathbf{b} \quad (38)$$

where

$$\mathbf{A} = \begin{bmatrix} \mathbf{A}_{LL} & \mathbf{A}_{LR} \\ \mathbf{A}_{RL} & \mathbf{A}_{RR} \end{bmatrix}. \quad (39)$$

The right-hand-side vector \mathbf{b} contains tested incident electric and magnetic fields

$$\mathbf{b} = [b_E^L \quad b_H^L \quad b_E^R \quad b_H^R \quad b_{E\sigma}^R]^T \quad (40)$$

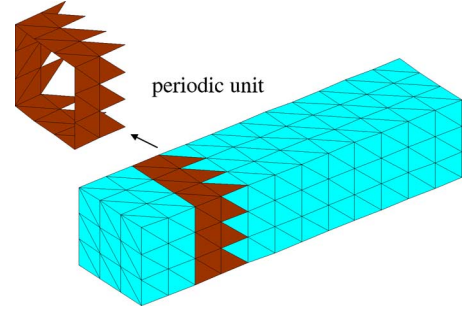


Fig. 11. Discretized waveguide with a periodic unit.

in which the n th entry of each subvector is given by

$$b_{E,n}^t = \int_S \mathbf{X}_n(\mathbf{r}) \cdot \mathbf{E}_{\text{inc}}^t(\mathbf{r}) dS \quad (41)$$

$$b_{H,n}^t = \int_S \mathbf{X}_n(\mathbf{r}) \cdot \mathbf{H}_{\text{inc}}^t(\mathbf{r}) dS \quad (42)$$

$$b_{E\sigma,n}^R = \int_S \sigma_E(\mathbf{r}) \mathbf{X}_n(\mathbf{r}) \cdot \mathbf{E}_{\text{inc}}^t(\mathbf{r}) dS. \quad (43)$$

B. Acceleration and Preconditioning With FFT

The linear system (38) can be solved with iterative algorithms, for instance, GMRES for this nonsymmetrically dense system. In each iteration, the matrix-vector product takes $O(N^2)$ time, where N is the number of unknowns. Moreover, to explicitly store the matrix \mathbf{A} is expensive, requiring $O(N^2)$ memory. In fact, there have been many well-developed fast algorithms to reduce the costs of the integral equation solvers [9]–[12]. In this paper, we use a straightforward and easily implemented FFT-based fast algorithm to accelerate the SIE method on periodic guided structures.

As shown in Fig. 11, the waveguide is discretized into a periodically repeating set of the RWG triangle pairs. Due to the mesh periodicity and the space invariance of the operators (34), (35), the matrices \mathbf{A}_{LL} and \mathbf{A}_{LR} are block Toeplitz, requiring explicit calculation and storage of only a block row and a block column, reducing memory to approximately $O(N)$. A Toeplitz matrix can be embedded in a circulant matrix, and the circulant matrix-vector product can be computed with the FFT [32], [33]. In this way, the computational costs are reduced approximately to $O(N \log N)$.

Because the surface conductivity σ_E must vary with distance from the waveguide-absorber interface, the tested potential operators (36), (37) are not space invariant. Therefore, accelerating the σ_E parameterized matrices \mathbf{A}_{RL} and \mathbf{A}_{RR} is not as straightforward as \mathbf{A}_{LL} and \mathbf{A}_{LR} . Typically, the integral in (36), (37) is calculated numerically using Gauss quadrature [34], summing up the tested potentials at quadrature (target) points with Gauss weights. The space invariance of the potential operators (31), (32) and periodicity of the mesh allows assembling a matrix of the potentials at target points by explicitly calculating only a block row and block column. Then the potentials at target points are summed after testing and multiplications with Gauss

weights and surface conductivity, and eventually stamped into matrices \mathbf{A}_{RL} and \mathbf{A}_{RR} .

Another great advantage of working with a Toeplitz or a block Toeplitz matrix is the existence of a highly efficient preconditioner [35]–[37]. A circulant matrix is approximated from the Toeplitz matrix, and then can be easily inverted with the FFT. We use this method to calculate a preconditioner for \mathbf{A}_{LL} , and use the block-diagonal preconditioner [12] for \mathbf{A}_{RR} .

REFERENCES

- [1] A. F. Oskooi, L. Zhang, Y. Avniel, and S. G. Johnson, "The failure of perfectly matched layers, and towards their redemption by adiabatic absorbers," *Opt. Exp.*, vol. 16, pp. 11376–11392, 2008.
- [2] R. F. Harrington, "Boundary integral formulations for homogeneous material bodies," *J. Electromagn. Waves Appl.*, vol. 3, no. 1, pp. 1–15, 1989.
- [3] K. Umashankar, A. Taflove, and S. M. Rao, "Electromagnetic scattering by arbitrary shaped three-dimensional homogeneous lossy dielectric objects," *IEEE Trans. Antennas Propag.*, vol. 34, no. 6, pp. 758–765, Jun. 1986.
- [4] S. M. Rao, D. R. Wilton, and A. Glisson, "Electromagnetic scattering by surfaces of arbitrary shape," *IEEE Trans. Antennas Propag.*, vol. AP-30, no. 3, pp. 409–418, May 1982.
- [5] C. F. Wang, F. Ling, and J. M. Jin, "A fast full-wave analysis of scattering and radiation from large finite arrays of microstrip antennas," *IEEE Trans. Antennas Propag.*, vol. 46, no. 10, pp. 1467–1474, Oct. 1998.
- [6] X. Q. Sheng, J.-M. Jin, J. Song, W. C. Chew, and C.-C. Lu, "Solution of combined-field integral equation using multilevel fast multipole algorithm for scattering by homogeneous bodies," *IEEE Trans. Antennas Propag.*, vol. 46, no. 11, pp. 1718–1726, Nov. 1998.
- [7] V. Rokhlin, "Rapid solution of integral equations of classical potential theory," *J. Comput. Phys.*, vol. 60, pp. 187–207, 1985.
- [8] R. L. Wagner and W. C. Chew, "A ray-propagation fast multipole algorithm," *Microw. Opt. Technol. Lett.*, vol. 7, pp. 435–438, 1994.
- [9] J. R. Phillips and J. K. White, "A precorrected-FFT method for electrostatic analysis of complicated 3-D structures," *IEEE Trans. Comput.-Aided Design*, vol. 16, no. 10, pp. 1059–1072, Oct. 1997.
- [10] Z. Zhu, B. Song, and J. White, "Algorithms in fastimp: A fast and wide-band impedance extraction program for complicated 3-D geometries," in *Proc. Design Automat. Conf. (DAC)*, 2003, pp. 712–717.
- [11] L. Zhang, N. Yuan, M. Zhang, L. W. Li, and Y. B. Gan, "RCS computation for a large array of waveguide slots with finite wall thickness using the mom accelerated by p-fft algorithm," *IEEE Trans. Antennas Propag.*, vol. 53, no. 9, pp. 3101–3105, Sep. 2005.
- [12] J. Song, C.-C. Lu, and W. C. Chew, "Multilevel fast multipole algorithm for electromagnetic scattering by large complex objects," *IEEE Trans. Antennas Propag.*, vol. 45, no. 10, pp. 1488–1493, Oct. 1997.
- [13] J. P. Berenger, "A perfectly matched layer for the absorption of electromagnetic waves," *J. Comp. Phys.*, vol. 114, pp. 185–200, 1994.
- [14] W. C. Chew and W. Weedon, "A 3-D perfectly matched medium from modified Maxwell's equations with stretched coordinates," *Microw. Opt. Technol. Lett.*, vol. 7, no. 13, pp. 599–604, 1994.
- [15] Z. S. Sacks, D. M. Kingsland, R. Lee, and J.-F. Lee, "A perfectly matched anisotropic absorber for use as an absorbing boundary condition," *IEEE Trans. Antennas Propag.*, vol. 43, no. 12, pp. 1460–1463, Dec. 1995.
- [16] S. D. Gedney, "An anisotropic perfectly matched layer-absorbing medium for the truncation of FDTD lattices," *IEEE Trans. Antennas Propag.*, vol. 44, no. 12, pp. 1630–1639, Dec. 1996.
- [17] A. Taflove, *Computational Electrodynamics: The Finite-difference Time-Domain Method*. Norwood, MA: Artech House, 1995.
- [18] M. Kuzuoglu and R. Mittra, "Frequency dependence of the constitutive parameters of causal perfectly matched anisotropic absorbers," *IEEE Microw. Guided Waves Lett.*, vol. 6, no. 12, pp. 447–449, Dec. 1996.
- [19] M. L. Povinelli, S. G. Johnson, and J. D. Joannopoulos, "Slow-light, band-edge waveguides for tunable time delays," *Opt. Exp.*, vol. 13, no. 18, pp. 7145–7159, 2005.
- [20] M. A. Popovic, M. R. Watts, T. Barwicz, P. T. Rakich, L. Socci, E. P. Ippen, F. X. Kartner, and H. I. Smith, "High-index-contrast, wide-FSR microring-resonator filter design and realization with frequency-shift compensation," presented at the Opt. Fiber Commun. Conf., Washington, DC, 2005.
- [21] D. Pissoor and F. Olyslager, "Termination of periodic waveguides by PMLs in time-harmonic integral equation-like techniques," *IEEE Antennas Wireless Propag. Lett.*, vol. 2, pp. 281–284, 2003.
- [22] D. H. Schaubert, D. R. Wilton, and A. W. Glisson, "A tetrahedral modeling method for electromagnetic scattering by arbitrarily shaped inhomogeneous dielectric bodies," *IEEE Trans. Antennas Propag.*, vol. AP-32, no. 1, pp. 77–85, Jan. 1984.
- [23] E. Erez and Y. Leviatan, "Electromagnetic scattering analysis using a model of dipoles located in complex space," *IEEE Trans. Antennas Propag.*, vol. 42, no. 12, pp. 1620–1624, Dec. 1994.
- [24] R. F. Harrington, *Time-Harmonic Electromagnetic Fields*. New York: McGraw-Hill, 1961.
- [25] L. Zhang, S. G. Johnson, and J. K. White, "Calculation of mie scattering from a sphere with surface conductivity using the boundary element method," *In Preparation*.
- [26] J. D. Joannopoulos, S. G. Johnson, J. N. Winn, and R. D. Meade, *Photonic Crystals: Molding the Flow of Light*, 2nd ed. Princeton, NJ: Princeton Univ. Press, 2008.
- [27] S. G. Johnson and J. D. Joannopoulos, "Block-iterative frequency-domain methods for Maxwell's equations in a planewave basis," *Opt. Exp.*, vol. 8, no. 3, pp. 173–190, 2001.
- [28] L. Zhang, J. K. White, and S. G. Johnson, "Absorbing terminations for periodic media in boundary element methods," 2010, to be published.
- [29] W. C. Chew, *Waves and Fields in Inhomogeneous Media*. New York: Van Nostrand, 1990.
- [30] A. Ishimaru, *Electromagnetic Wave Propagation, Radiation, and Scattering*. Englewood Cliffs, NJ: Prentice-Hall, 1991.
- [31] R. F. Harrington, *Field Computation by Moment Methods*. New York: Macmillan, 1968.
- [32] C. V. Loan, "Computational frameworks for the fast Fourier transform," Society for Industrial and Applied Mathematics 1992.
- [33] Y. Zhuang, K. L. Wu, C. Wu, and J. Litva, "A combined full wave CGFFT method for rigorous analysis of large microstrip antenna arrays," *IEEE Trans. Antennas Propag.*, vol. 44, no. 1, pp. 102–109, Jan. 1996.
- [34] L. N. Trefethen and D. Bau, *Numerical Linear Algebra*. Philadelphia, PA: SIAM, 1997.
- [35] G. Strang, "A proposal for Toeplitz matrix calculations," *Stud. Appl. Math.*, vol. 74, pp. 171–176, 1986.
- [36] T. F. Chan, "An optimal circulant preconditioner for Toeplitz systems," *SIAM J. Sci. Statist. Comput.*, vol. 9, no. 4, pp. 766–771, 1988.
- [37] T. F. Chan and J. A. Olkin, "Circulant preconditioners for Toeplitz-block matrices," in *SIAM Conf. Linear Algebra Signals, Syst., Control*, 1990, pp. 89–101.

Lei Zhang (S'04) received the B.Eng. degree in electrical engineering from the University of Science and Technology of China, Hefei, China, in 2003, the M.Eng. degree in electrical and computer engineering from the National University of Singapore, Singapore, in 2005, the M.S. degree in computational design and optimization, and the Ph.D. degree in electrical engineering from the Massachusetts Institute of Technology, Cambridge, in 2007 and 2010, respectively. He received Mathworks fellowship in 2006. His research interests include numerical modeling, computational electromagnetics, and nanophotonics.

Jung Hoon Lee received the B.S. and M.S.E. degrees in electrical engineering from the Korea Advanced Institute of Science and Technology, Daejeon, South Korea, in 1999 and 2001, respectively, the M.S. degree in high-performance computation for engineered systems from the National University of Singapore, Singapore, in 2001, and the Ph.D. degree in electrical engineering and computer science from the Massachusetts Institute of Technology, Cambridge, in 2008. He is currently a Research Associate at Merck & Company, Inc., Rahway, NJ, working on physiological models and population pharmacokinetic-pharmacodynamic models.

Ardavan Oskooi received the Bachelor's (Hons.) degree in engineering science from the University of Toronto, Toronto, ON, Canada, in 2004, and the M.Sc. degree in computation for design and optimization and the D.Sc. degree in materials science and engineering, from Massachusetts Institute of Technology, Cambridge, in 2008 and 2010, respectively.

He is currently a Postdoctoral Fellow at Kyoto University, Kyoto, Japan.

Amit Hochman received the B.Sc., M.Sc., and Ph.D. degrees in electrical engineering from the Technion-Israel Institute of Technology, Haifa, Israel in 1996, 2005, and 2009, respectively.

He is currently a Postdoctoral Fellow in the Computational Prototyping Group, Massachusetts Institute of Technology, Cambridge. In his research as a graduate student, he developed software packages for analysis of photonic-crystal fibers and plasmonic waveguides, as well as for fast evaluation of Sommerfeld integrals. From 1997 to 2002, he was in military service where he engaged on the simulation of adaptive antennas and communication systems. His research interests include computational electromagnetics, and model-order reduction for microelectromechanical systems and nonlinear circuits.

Jacob K. White (F'08) received the B.S. degree in electrical engineering and computer science from the Massachusetts Institute of Technology (MIT), Cambridge, in 1980, and the S.M. and Ph.D. degrees in electrical engineering and computer science from the University of California, Berkeley, in 1983 and 1985, respectively.

He was at the IBM T. J. Watson Research Center from 1985 to 1987, was an Analog Devices Career Development Assistant Professor at MIT from 1987 to 1989, and became a Presidential Young Investigator in 1988. He is currently a C. H. Green Professor in Electrical Engineering and Computer Science at MIT. He is best known for supervising the development of the interconnect analysis programs Fastcap and Fasthenry, for his collaboration on the development of the algorithms in Spectre and SpectreRF, and for his students' work on linear, nonlinear and parameterized model reduction. His research interests include numerical algorithms for the simulation and optimization of circuits, interconnect, nanophotonics, bioMEMS and NEMS, bio molecules, and network models of biological systems.

Dr. White was an Associate Editor of the IEEE TRANSACTIONS ON COMPUTER-AIDED DESIGN from 1992 to 1996, served as the Chair for the International Conference on Computer-Aided Design in 1999.

Steven G. Johnson received the B.S. degree in physics, mathematics, and electrical engineering and computer science from the Massachusetts Institute of Technology (MIT), Cambridge, in 1995, and the Ph.D. degree in physics from the same institute, in 2001, for his work on the theory of photonic crystals.

Since 2004, he has been a Faculty Member of the Department of Mathematics, MIT. He was a co-recipient of the 1999 J. H. Wilkinson Prize for Numerical software for his work on the FFTW fast Fourier transform library, and is also the author or coauthor of several other widely used software packages in photonics simulation. His research interests include nanophotonic devices and modeling, the theory of waves in inhomogeneous media, computational methods for simulation and design, and effects of quantum electrodynamic fluctuations.